

# Mechanics of Wide-flanged Steel Sections that Develop Thermal Gradients Due to Fire Exposure

Maria E. M. Garlock\* and Spencer E. Quiel

Department of Civil and Environmental Engineering, Princeton University, Princeton, NJ 08544 USA

---

## Abstract

This paper examines the behavior of wide-flanged (WF) steel sections with axial load and a thermal gradient through the section depth due to uneven exposure to fire. Such conditions may produce a shift of the section's effective centroid (i.e. the center of stiffness), which will move away from the section's geometric centroid toward the cooler side. If the axial loads carried by the section are applied at its geometric centroid (as is typically assumed), the presence of a thermal gradient produces a bending moment because the axial loads are now acting eccentrically to the section's effective centroid. These moments become large enough to reverse the direction of moment in the member. This paper describes the mechanics of this behavior in detail and evaluates the effects of different levels of axial load on the magnitude of the centroidal shift and on the moments that develop as a result. It is observed that larger axial loads produce larger shifts of the effective centroid, and yet the total moment in the section becomes smaller.

**Keywords:** fire, steel, temperature gradient, plastic P-M interaction curve, plastic neutral axis, plastic centroid

---

## 1. Introduction

Current practice for the design of steel members exposed to fire typically calculates the capacity and performance of these members by assuming uniform temperature through the section depth. This assumption may be an acceptable approximation if the member is heated on all sides, as in the case of an interior column in a building. However, in some cases, such as a column on the perimeter of the building or a beam supporting a slab, only three sides of the section are exposed to fire and a thermal gradient will form through the section's depth. As the section temperatures become high enough to reduce the material properties, the section will develop an asymmetric distribution of strength and stiffness. The uneven strength distribution will alter the plastic capacity of a section carrying a combination of axial load and moment (Garlock and Quiel, 2006). The uneven stiffness distribution will cause the center of stiffness (i.e. the "effective centroid") of the section to move away from its geometric centroid. An axial load applied at the geometric centroid will therefore be applied eccentric to the effective centroid, thereby generating moment about the geometric centroid.

Recent fire-induced structural collapses such as the Windsor Tower in Madrid (Fletcher *et al.*, 2006) and the

World Trade Center Twin Towers (Usmani *et al.*, 2003; Gann, 2005) justify the need for a better understanding of the fire induced response of structures. In both of these events, the perimeter columns, which were likely subject to thermal gradients at some point during the fire, played a role in the eventual collapse. Previous publications by other researchers have noted that thermal gradients produce a shift of the effective centroid (Wang, 2002; El-Rimawi *et al.*, 1995), but none have yet described in detail the exact mechanics regarding the shift of the effective centroid's location. This paper describes the effects of this centroidal shift on the structural performance and capacity of wide-flanged (WF) steel sections that develop a thermal gradient due to uneven fire exposure. It examines the effects of the magnitude of applied load and compares the responses of a thermal gradient parallel to the web (which leads to strong axis bending) to a gradient parallel to the flange (which leads to weak axis bending).

## 2. Definition of Terms

Before we proceed with a discussion of the mechanics of steel WF sections with thermal gradients, the definitions of the following four terms are given for clarity: (1) geometric centroid, (2) effective centroid, (3) plastic centroid, and (4) plastic neutral axis.

### 2.1. Geometric centroid

The geometric centroid (GC) of a cross-section

---

\*Corresponding author

Tel: +1-609-258-2728, Fax: +1-609-258-1563

E-mail: mgarlock@princeton.edu, squiel@princeton.edu

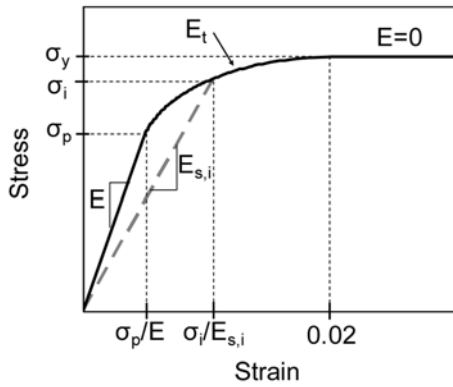


**Figure 1.** Non-linear material model for steel with temperature greater than 100°C (CEN, 2001).

represents the center of the section's geometry. Because steel WF sections have symmetric cross-sectional areas, the GC will be located at the mid-depth of the section (i.e. at the center of the web). The location of the GC remains unchanged when a section is exposed to fire because its physical geometry is not altered by any fluctuation in the steel material's temperature, strength, or stiffness.

## 2.2. Effective centroid

The effective centroid (EC) represents the center of stiffness in a steel cross-section. It is the location through which the axial load must be applied to produce pure axial stress with no bending. Fig. 1 defines the non-linear material properties of steel at elevated temperatures according to Eurocode (CEN, 2001). When the stress in the steel,  $\sigma$ , exceeds the proportional limit stress,  $\sigma_p$ , the material becomes non-linear. At a strain of 0.02,  $\sigma$  equals the yield stress ( $\sigma_y$ ). Eurocode assumes that  $\sigma_y$  is reduced from its value at ambient temperature ( $\sigma_{y,20}$ ) when the steel material temperature exceeds 400°C. It also assumes that the material is elastic-perfectly-plastic (i.e.  $\sigma_p = \sigma_y$ ) until temperatures exceed 100°C. To determine the EC of a section with a non-uniform temperature distribution (in which both the elastic and inelastic regimes may be present), the secant modulus,  $E_{s,i}$  is used as a generalized description of stiffness (El-Rimawi *et al.*, 1995; Burgess *et al.*, 1990).

$$E_{s,i} = \frac{\sigma_i}{\varepsilon_i} \quad (1)$$

The subscript  $i$  refers to fiber  $i$  of a discretized steel cross-section. Likewise,  $\sigma_i$  and  $\varepsilon_i$  refer to the stress and strain, respectively, experienced by fiber  $i$ . Fig. 1 shows the secant modulus as a direct ratio of stress and strain.  $E_{s,i}$  equals the initial modulus of elasticity,  $E$ , when the fiber has not undergone any inelastic deformation. Beyond this point,  $E_{s,i}$  does not represent the true stiffness of each fiber, but this is not relevant since we are essentially using  $E_{s,i}$  as a relative measure of stiffness among the fibers and as a means to calculate  $\sigma_i$ . The location of the EC ( $y_{EC}$ ) may therefore be obtained via the

following expression:

$$y_{EC} = \frac{\sum E_{s,i} y_i A_i}{\sum E_{s,i} A_i} \quad (2)$$

where  $A_i$  is the area of fiber  $i$  and  $y_i$  is the distance of fiber  $i$  from the reference axis. In this study, we have selected the GC as the reference axis since this location does not move when the section is exposed to fire. In addition, the GC is the location typically used as a reference axis in computational tools. Eq. (2) shows that  $y_{EC}$  is a function of both the section's temperature and applied stress since  $E_{s,i}$  will vary with both.

## 2.3. Plastic centroid

The plastic centroid (PC) represents the location through which the resultant of axial force must be applied to a fully yielded (i.e. plastic) cross-section in order to produce pure axial stress with no bending. The location of the PC ( $y_{PC}$ ) is therefore the position of the stress resultant in a cross-section that has reached full yield in uniform compression or tension, and it is obtained by solving the following summation:

$$y_{PC} = \frac{\sum \sigma_{y,i} y_i A_i}{\sum \sigma_{y,i} A_i} \quad (3)$$

where  $\sigma_{y,i}$  is the yield stress at fiber  $i$ . The denominator of Eq. (3) represents the section's yield force capacity,  $P_y$ . For a WF steel section with uniform  $\sigma_y$ , the stress distribution corresponding to full yield in pure compression or tension will be symmetric, and therefore the PC will coincide with the GC. In the case of a WF section with exposure to fire on three sides (Fig. 2(a)), the section develops an uneven temperature profile as shown in Fig. 2(b). If the temperatures are large enough, the section will also develop an uneven  $\sigma_y$  profile, as seen in Fig. 2(c). For example, if using the Eurocode model, the uneven  $\sigma_y$  profile will develop once the temperature in any of the fibers exceeds 400°C (i.e. once  $\sigma_y < \sigma_{y,20}$ ). Fig. 2(c) shows that the resultant of the compressive stresses,  $C$ , is acting at the PC, which lies above the GC. Since the cooler top flange has a greater overall  $\sigma_y$  than the hotter lower flange, the resultant of the  $\sigma_y$  distribution will shift from the GC toward the top flange according to Eq. (3). As seen in Eq. (3),  $y_{PC}$  is only a function of temperature since it is the only parameter that affects  $\sigma_y$ .

## 2.4. Plastic neutral axis

The plastic neutral axis (PNA) represents the neutral axis position about which the resultants of the compressive and tensile stresses in a fully yielded section are equal (i.e.  $C = T$ ) as shown in Fig. 2(d). The PNA location is calculated by finding the neutral axis position at which the total axial load  $P$  in the yielded section is zero:

$$P = \int_A \sigma_y dA = \sum \sigma_{y,i} A_i = 0 \quad (4)$$

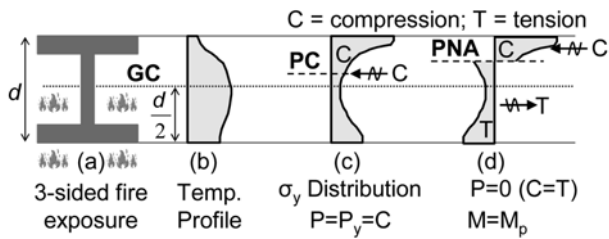


**Figure 2.** Stress profiles, based on the (a) section and (b) temperature profiles provided, describing the (c) plastic centroid (PC) and (d) plastic neutral axis (PNA).

The section's plastic moment,  $M_p$ , may be calculated at this neutral position by integrating the yield stress (with the appropriate sign for compression or tension) times area in every fiber times its distance to a reference axis:

$$M_p = \int_A \sigma_y y dA = \sum \sigma_{y,i} y_i A_i = 0 \quad (5)$$

In this case,  $y_i$  is the distance from fiber  $i$  to the reference axis.

### 3. Isolated Column Study

For clarity and simplicity, we begin by studying the behavior of a column section in isolation. In a later section of this paper we will examine this column as it interacts with other members in a frame. Using a column in isolation provides a clearer approach to understanding the mechanics of steel sections with thermal gradients. The model used in this study is shown in Fig. 3(a). The column is restrained from rotating at its top and bottom and will therefore develop a uniform moment along its length. The top end is allowed to translate vertically so as not to restrain axial thermal expansion; therefore, axial load  $P$  remains constant for the duration of the fire. The WF column is subjected to the fire curve shown in Fig. 3(b), and this fire is applied on three sides of the cross-section as shown by the dotted lines on the cross-section in Fig. 3(a). The fourth side is represented as an adiabatic surface. Since the fire is applied on three sides of the cross-section, a non-uniform thermal gradient (which has a similar profile during most of the fire as that shown in Fig. 2(b)) develops through the section's depth. Such an analysis may represent a column located in the perimeter of a building frame. Note that if the fourth side was instead modeled as capable of heat loss, a thermal gradient would still emerge and the conclusions of this paper would be the same. The column section and fire curve are taken from a previous study of a real fire event conducted by the authors (Garlock and Quiel, 2007).

The column section has a low slenderness, and therefore flexural buckling is precluded as a limit state (Garlock and Quiel, 2007). Local buckling is not considered in this study. Second order *frame* ( $P-\Delta$ ) effects are not considered because the column studied here does not

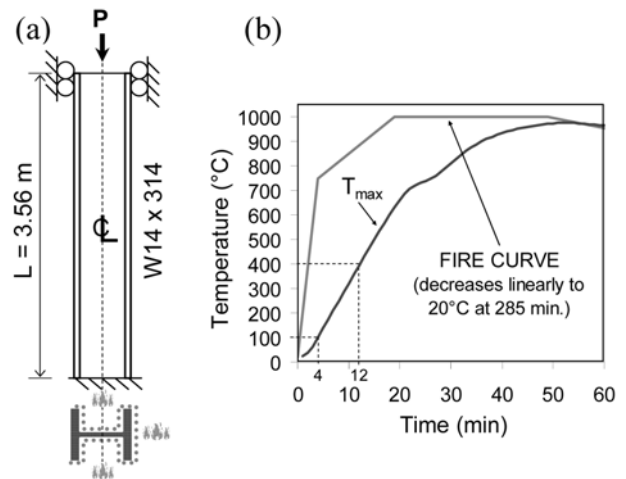


**Figure 3.** Prototype for the (a) column and (b) fire curve used for this study, also shown with maximum temperature ( $T_{max}$ ) in the column.

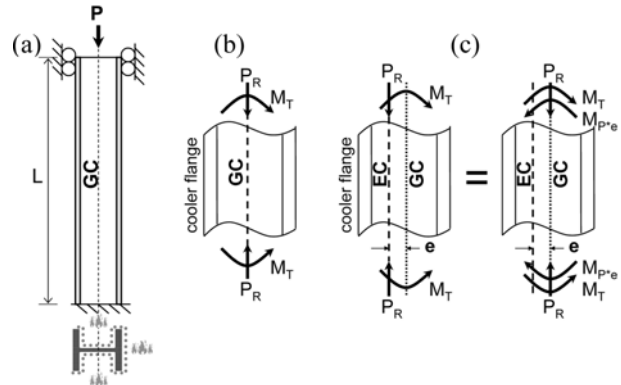


**Figure 4.** Behavior of a column (a) exposed to fire on three sides whose internal  $P$  and  $M$  are shown (b) before and (c) after the section's centroid begins to move.

deflect laterally at its supports. Analyses show that when the column is modeled in a full frame, the expanding beam will push out the perimeter column; however, the beam acts as a tension strut and makes the  $P-\Delta$  effects on the column negligible. Second order *member* ( $P-\delta$ ) effects are considered in the finite element analyses discussed in this paper, but these effects are negligible due to the high flexural stiffness of the member chosen. Note that for columns with smaller flexural stiffness,  $P-\delta$  effects may amplify the column's bending moment.

Fig. 4 shows the behavior of a column with a thermal gradient in the direction parallel to the web. The sign convention for this study is such that positive moments produce tension in the left-hand (cooler) face of the member, and positive axial forces correspond to compression. Initially, the column will develop a bending moment in response to the thermal strains induced by the gradient because the column ends are fixed against rotation. Since the right face is hotter than the left face, the right face will undergo a larger thermal expansion. If

the column ends were free to rotate, the column would therefore bow to the right. Since the ends are restrained from rotating, the right face becomes compressed and the left face experiences tension. This reaction creates a positive bending moment according to our sign convention. This “thermal” moment is referred to as  $M_T$  and is shown in Fig. 4(b).

Before the increasing temperatures affect the steel material properties, the position of the EC coincides with the GC, as shown in Fig. 4(b). When the temperatures in the section have increased so that the material properties ( $E$ ,  $s_y$ , and  $s_p$ ) have reduced, the EC begins to migrate towards the cooler flange as shown in Fig. 4(c). The resultant of the axial stresses ( $P_R$ ) in the section must equal the applied load,  $P$ , to maintain equilibrium. The position of  $P$  does not move, but the position of  $P_R$  (which is located at the EC) moves according to the change in the section’s material properties. The movement of  $P_R$  generates an additional moment about the GC,  $M_{P^*e}$ , that is equal to  $P$  times the distance,  $e$ , from the GC to the new position of the EC (as shown in Fig. 4(c)).  $M_{P^*e}$  is opposite in direction to  $M_T$ . It is therefore expected that during some point in the fire, the total moment will first reverse its direction (when the rate of increase of  $M_{P^*e}$  becomes larger than that of  $M_T$ ) and then reverse its sign (when  $M_{P^*e}$  itself becomes larger than  $M_T$ ).

To calculate  $M_T$ , one needs to determine the mechanical (or stress-related) strains induced via resistance to thermal curvature at every fiber  $i$  ( $\varepsilon_{\sigma,T,i}$ ). The total strain of every fiber ( $\varepsilon_{total}$ ) is comprised of the mechanical strain ( $\varepsilon_{\sigma,i}$ ) plus the thermal strain ( $\varepsilon_{T,i}$ ), which equals the coefficient of thermal expansion times the change in the fiber’s temperature ( $\sigma T_i$ ). Note that  $\varepsilon_{total}$  does not have a subscript  $i$ . For the column shown in Fig. 3, the rotation of each end is restrained, and therefore  $\varepsilon_{total}$  will be constant as the top face remains horizontal and all fibers translate uniformly in the vertical direction. In the structural-thermal analysis described by Fig. 3,  $\varepsilon_{\sigma,i}$  is comprised of  $\varepsilon_{\sigma,T,i}$  plus  $\varepsilon_{\sigma,P,i}$  which is the mechanical strain induced by applied load  $P$ . The stress at every fiber  $i$ ,  $\sigma_i$ , equals  $\varepsilon_{\sigma,i}$  times secant modulus  $E_{s,i}$ .  $E_{s,i}$  is obtained from the results of the analysis that is illustrated in Fig. 3, which considers the combined effects of thermal and structural loading. The relationships described above can be expressed as:

$$\varepsilon_{total} = \varepsilon_{\sigma,i} + \varepsilon_{T,i} \quad (6)$$

$$\varepsilon_{\sigma,i} = \varepsilon_{\sigma,T,i} + \varepsilon_{\sigma,P,i} \quad (7)$$

$$\sigma_i = \varepsilon_{\sigma,i} E_{s,i} \quad (8)$$

We can solve for  $\varepsilon_{\sigma,T,i}$  by setting  $P=0$ , thereby eliminating  $\varepsilon_{\sigma,P,i}$  and creating the following relationship using Eqs. (6) and (7):

$$\varepsilon_{\sigma,i} = \varepsilon_{\sigma,T,i} = \varepsilon_{total} - \varepsilon_{T,i} \quad (9)$$

Internal force equilibrium must be maintained, therefore, by summing over each fiber  $i$ :

$$P = \sum \varepsilon_{\sigma,T,i} E_{s,i} A_i = \sum (\varepsilon_{total} - \varepsilon_{T,i}) E_{s,i} A_i = 0 \quad (10)$$

$\varepsilon_{T,i}$  can be obtained from the results of thermal finite element analysis.  $E_{s,i}$ , as noted previously, corresponds to the stiffness of the column under combined thermal and structural loading when  $P$  is not equal to zero (i.e. when  $P$  equals its original value). Since  $\varepsilon_{total}$  is constant for every fiber in the column shown in Fig. 3, we can solve for it using Eq. (10):

$$\varepsilon_{total} = \frac{\sum \varepsilon_{T,i} E_{s,i} A_i}{\sum E_{s,i} A_i} \quad (11)$$

The thermal moment,  $M_T$ , may then be calculated using the following expression, in which all variables needed to obtain the solution are now known:

$$M_T = \sum \varepsilon_{\sigma,T,i} E_{s,i} y_i A_i = \sum (\varepsilon_{total} - \varepsilon_{T,i}) E_{s,i} y_i A_i = 0 \quad (12)$$

This equation is validated later in this paper with finite element results of structural-thermal analysis.

### 3.1. Applied P = 25% of initial P<sub>y</sub>

Our first case in the isolated column study examines the results for finite element solutions of the structure shown in Fig. 3 with applied  $P = 25\%$  of the initial  $P_y$ . Computational modeling for this study was performed using SAFIR, a software developed at the University of Liege that is specifically designed for structures exposed to fire (Franssen, 2005). The computational structural model representing the column shown in Fig. 3(a) is discretized into ten beam elements. The column’s cross-section was discretized into several fibers. The flange plates were modeled with four fibers through the thickness and twenty-four fibers along the width. The web plate had two fibers through the thickness and twenty fibers along the height. The material properties at high temperatures were based on Eurocode (CEN, 2001), where  $E$  and  $s_p$  begin to decrease at 100°C and  $s_y$  begins to decrease at 400°C. The positions of the effective centroid, plastic centroid, and plastic neutral axis (i.e.  $y_{EC}$ ,  $y_{PC}$ , and  $y_{PNA}$ ) are shown in Fig. 5(a). For reasons described previously, the zero reference position, is the GC. The shaded region in Fig. 5(a) is a sketch of the top half of the steel section, where it can be seen that the underside of the top flange is located at 177 mm.

Initially, the section’s stiffness and  $s_y$  profiles are uniform, and thus the EC, PC and PNA will coincide with the GC due to the section’s symmetry. Fig. 5(a) shows how each of these positions moves up, towards the cooler flange, as time progresses.  $y_{EC}$  is calculated at every time step using Eq. (2). The values of  $E_{s,i}$  for Eq. (2) is calculated using Eq. (1), where  $\varepsilon_i$  and  $\sigma_i$  are outputs of structural analysis in SAFIR. The EC does not move from the GC until the temperature in the hottest fibers in the steel section exceeds 100°C (i.e., when the section’s total

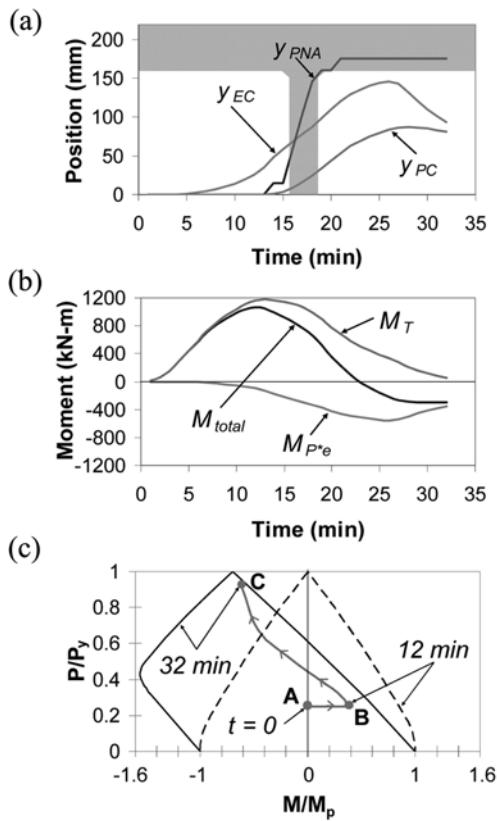


**Figure 5.** Plots of (a) centroidal location, (b) moment components, and (c) normalized  $P$ - $M$  performance for a  $W14 \times 314$  column subjected to fire on three sides and applied  $P = 25\%$  of initial  $P_y$ .

stiffness becomes non-uniform), shown to occur in Fig. 3(b) after  $t = 4$  minutes. Likewise, the PC and PNA do not move from the GC until the temperature in the hottest fibers exceeds  $400^\circ\text{C}$  (i.e., when the section's  $s_y$  profile becomes non-uniform), shown to occur in Fig. 3(b) after  $t = 12$  minutes. At about 20 minutes, the PNA is in the flange. As heat continues to conduct through the section toward the cooler unexposed face, the thermal gradient decreases after  $t = 26$  minutes and thus the difference in  $E_{s,i}$  between the fibers in the cooler and hotter regions also decreases. At this time, the position of the EC as calculated by Eq. (2) therefore begins to shift back toward the hotter region. As the section becomes plastic and approaches its yield capacity (i.e. when the column “fails” at  $t = 32$  minutes), the position of its EC converges to that of the PC.

As described previously, the total moment acting on the section ( $M_{total}$ ) is composed of  $M_T$  and  $M_{P^*e}$ . The magnitude of these components is shown in Fig. 5(b).  $M_{P^*e}$  in the analysis is obtained by multiplying  $P$  by the eccentricity  $e$  (shown in Fig. 5(a)), which is equal to  $y_{EC}$  (from Fig. 5(a)).  $M_{total}$  is obtained from structural analysis in SAFIR, and  $M_T$  is obtained using Eq. (12). This equation is validated in Fig. 5(b) since the summation of  $M_T$  and  $M_{P^*e}$  equals  $M_{total}$ .

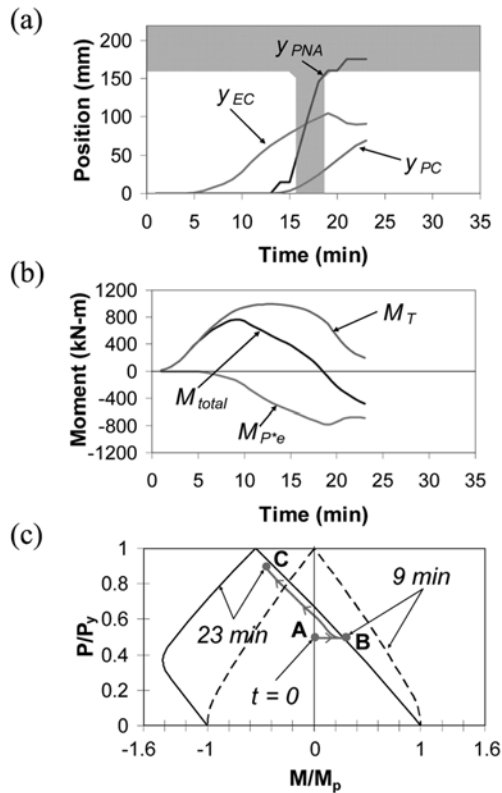
The behavior described by Fig. 4 is consistent with Fig 5(b): at  $t = 5$  minutes,  $e$  (i.e.  $y_{EC}$ ) moves towards the cooler flange and  $M_{P^*e}$  develops in the section. At this time, the total moment in the section begins to increase at a decreasing rate. At  $t = 12$  minutes,  $M_{total}$  peaks and begins to reverse direction as the rate of increase of  $M_{P^*e}$  becomes larger than the rate of increase of  $M_T$ . Eventually,  $M_{P^*e}$  becomes larger than  $M_T$  and  $M_{total}$  reverses sign at  $t = 23$  minutes.

Fig. 5(c) shows the interaction of  $P$  and  $M$ , where  $M = M_{total}$  and  $P$  and  $M$  are normalized by the temperature-dependent  $P_y$  and  $M_p$ , respectively, at every time step in the analysis. Positive values for  $P$  denote compression. The curve of combined  $P/P_y$  and  $M/M_p$  moves with time in the analysis, as marked in the Fig. 5(c), from point A to point B to point C. The plastic  $P$ - $M$  interaction curves are drawn for the times related to points B and C. These curves represent the boundary of the yield capacity of the section and are derived based on methods described by (Garlock and Quiel, 2006). Fig. 5(c) shows that at 12 minutes (point B), the moment reverses direction. This is the same time at which  $M_{total}$  in Fig. 5(b) peaks and begins to decrease. Point B is well inside the 12 minute plastic  $P$ - $M$  interaction curve, and thus the moment reversal is due solely to the increase of  $M_{P^*e}$ . Fig. 5(c) also shows a steady increase in  $P/P_y$  after 12 minutes that is due to a thermally induced decrease of the section's  $P_y$ . The analysis continues as the moments change sign, becoming negative until eventually the plastic  $P$ - $M$  interaction curve is reached at 32 minutes (point C) and the analysis terminates (i.e. convergence can no longer be attained as the section fully yields).

### 3.2. Effects of increasing applied $P$

Figs. 6 and 7 show similar plots as Fig. 5 for column cases with applied  $P = 50\%$  and  $75\%$  of the initial  $P_y$ , respectively. Together, Figs. 5, 6, and 7 show the effects of applied axial load on the behavior of columns with thermal gradients. Comparing Figs. 5(a), 6(a), and 7(a), it is seen that the rate at which  $y_{EC}$  moves from the GC (toward the cooler flange) increases with a larger applied  $P$ . Larger applied  $P$  creates larger initial stress and strain in the section, and some fibers will therefore go into the inelastic regime earlier in the analysis (once their steel material becomes non-linear at about 5 minutes). The ratio of stress to strain (i.e. the secant modulus) in these fibers becomes smaller because the increase of inelastic strain is significantly greater than a corresponding increase in stress, as seen in Fig. 1. Therefore, at any given time,  $y_{EC}$  will be greater in the column with the larger applied  $P$  and increase at a faster rate. Figs. 5(a), 6(a), and 7(a) also show that  $y_{PC}$  and  $y_{PNA}$  are not affected by the magnitude of applied  $P$  since their position is only a function of temperature.

Figs. 5(b), 6(b), and 7(b) show that  $M_{P^*e}$  ( $= P * e$ ) increases at a faster rate with a larger applied  $P$ . This occurs for two reasons: (1) a larger  $P$ , and (2) a larger  $y_{EC}$



**Figure 6.** Plots of (a) centroidal location, (b) moment components, and (c) normalized  $P-M$  performance for a  $W14 \times 314$  column subjected to fire on three sides and applied  $P = 50\%$  of initial  $P_y$ .

at each time step as described previously (where  $e = y_{EC}$ ). Figs. 5(b), 6(b), and 7(b) also show the effects of applied  $P$  on  $M_T$ , where it is seen that  $M_T$  decreases with increasing applied  $P$ . The fibers in the section accumulate inelastic strain at a faster rate with larger applied  $P$ , as described previously, causing  $E_s$  in the inelastic fibers to decrease. Therefore,  $M_T$  will also decrease with larger applied  $P$  since the solution for  $M_T$  is a function of the  $E_s$  in each fiber (as shown in Eq. (12)). As  $M_{P^*e}$  becomes larger and  $M_T$  becomes smaller with larger applied  $P$ , the maximum value of  $M_{total}$  will generally become smaller with larger applied  $P$  as these two moment components counteract each other. This trend can be seen clearly in Figs. 5(b), 6(b), and 7(b).

The plots of normalized  $P-M$  behavior in Figs. 6(c) and 7(c) show similar trends as that in Fig. 5(c) for greater initial values of applied  $P$ . From Point A to Point B, the moment ratio increases positively due to an increase of  $M_T$ . In all of the analysis cases considered, Point B is within the plastic  $P-M$  interaction curve for the column section at the corresponding time. Point B, representing the peak  $M/M_p$ , is reached earlier in the analysis with a larger applied  $P$  since  $M_{P^*e}$  is increasing faster. From Point B to Point C, the moment reverses direction due to an increase of  $M_{P^*e}$  and the  $P/P_y$  ratio increases due to a thermally induced reduction of  $P_y$  until the plastic  $P-M$

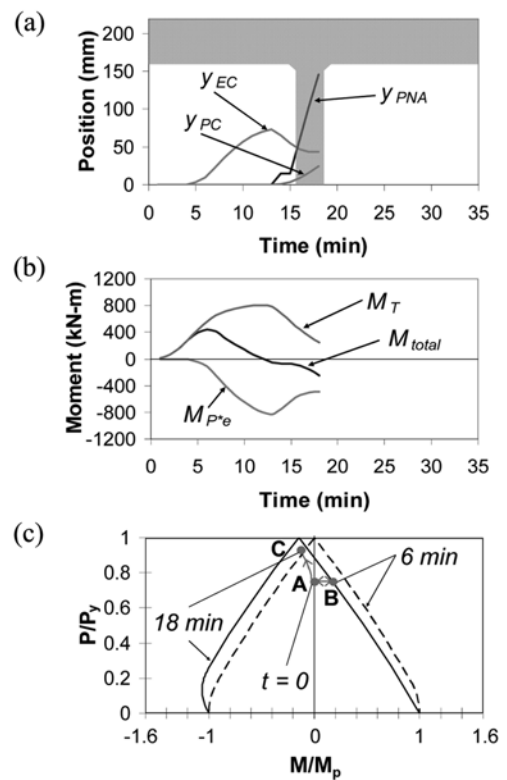


**Figure 7.** Plots of (a) centroidal location, (b) moment components, and (c) normalized  $P-M$  performance for a  $W14 \times 314$  column subjected to fire on three sides and applied  $P = 75\%$  of initial  $P_y$ .

interaction curve is reached at Point C. As expected, Point C is reached earlier in the analysis with larger applied  $P$ .

### 3.3. Effects of gradient orientation

All of the column cases discussed thus far have considered the three-sided fire exposure as inducing moment about the strong axis of the WF member. Here we consider a column with fire exposure on three sides such that the member will experience moment about its weak axis. The “strong axis” and “weak axis” fire exposure orientations are shown in the section profile inserts in Fig. 8(a). The strong axis exposure is the same as previously described. The weak axis exposure considers the fire to be applied to the outside of the flanges and one side of the web, as shown by the dotted lines. As before, the side of the member not exposed to fire is modeled as an adiabatic surface. Figs. 8(a) and 8(b) show the thermal gradient and  $\epsilon_y$  distribution over the normalized section profile for each case (shown at  $t = 25$  minutes as a representative time). The strong axis case has a temperature bulge in the web plate because it is thin relative to the flanges. The weak axis case has a more linear gradient than the strong axis case since its gradient is parallel to the flanges, which have more mass than the web and therefore heat more gradually.

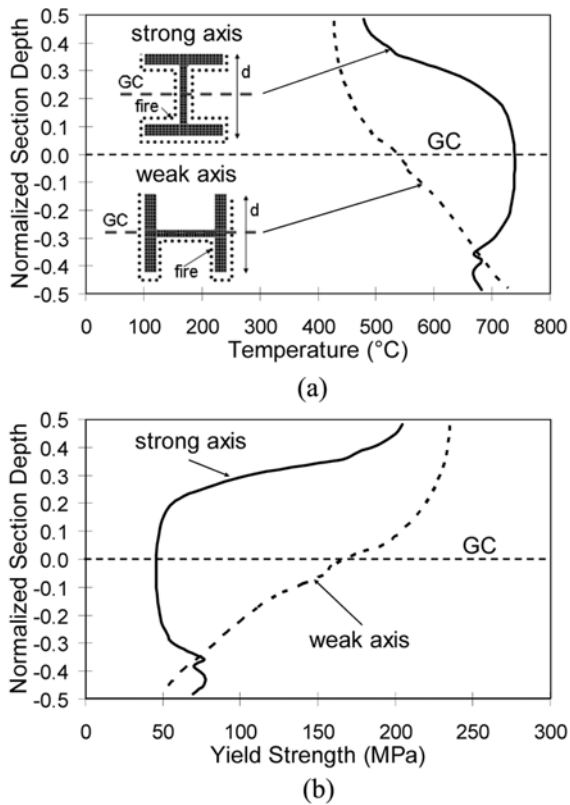


**Figure 8.** Comparison of (a) temperature and (b) yield strength profiles over the normalized section depth for W14 x 314 sections with strong and weak axis loading at  $t = 25$  minutes.

Fig. 9 describes the structural behavior, using plots similar to those in Figs. 5-7, of the column shown in Fig. 3 (with applied  $P = 25\%$  initial  $P_y$ ) for three-sided weak axis fire exposure. Fig. 9(a) shows that  $y_{EC}$ ,  $y_{PC}$ , and  $y_{PNA}$  all show similar trends as in Fig. 5 but with smaller magnitudes and slower rates of movement away from the GC toward the cooler side of the section. The centroidal shifts are smaller and slower in this case because the weak axis radius of gyration, which represents the concentration of material area in a cross-section about the section's GC, is smaller than that for the strong axis case. The performance of a heated WF section is typically governed by its flanges because they constitute the bulk of the section's mass. In the weak axis case, the flanges' center of mass is on the GC, as opposed to the strong axis case where the flanges are distant to the GC. Therefore, a change in flange temperature in the weak axis case will have less effect on  $y_{EC}$ ,  $y_{PC}$ , and  $y_{PNA}$ .

Fig. 9(b) shows that the trends of  $M_{P^*e}$ ,  $M_T$ , and  $M_{total}$  are similar for the weak axis case as they are for the strong axis case (as shown in Fig. 5(b)). However,  $M_{P^*e}$  is smaller for the weak axis case due to a smaller  $y_{EC}$ .  $M_T$  is also smaller for the weak axis section because the weak section has a smaller radius of gyration, as discussed above. Since  $M_{P^*e}$  and  $M_T$  are smaller,  $M_{total}$  is therefore smaller.

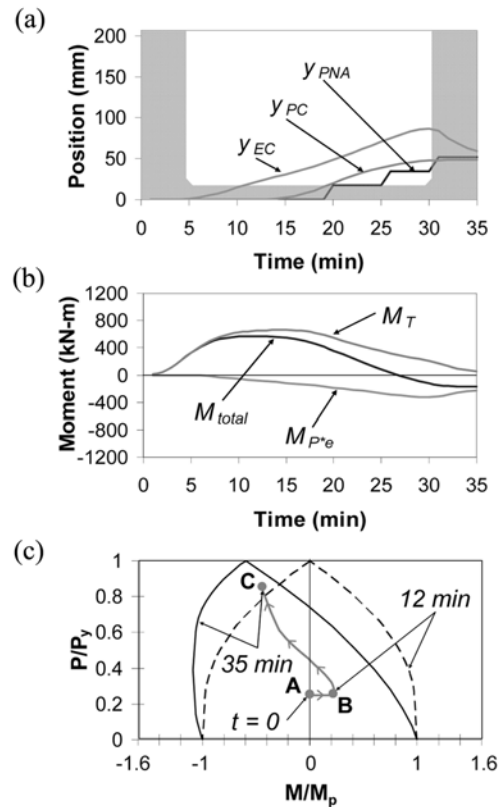


**Figure 9.** Plots of (a) centroidal location, (b) moment components, and (c) normalized  $P$ - $M$  performance for a W14 x 314 column subjected to fire on three sides (weak axis exposure) and applied  $P = 25\%$  of initial  $P_y$ .

Fig. 9(c) shows that the  $P$ - $M$  behavior of a column with weak axis exposure will experience a moment reversal before it reaches the plastic  $P$ - $M$  interaction curve. Increases in  $M/M_p$  and  $P/P_y$  push the section toward reaching its  $P$ - $M$  yield capacity. The mechanics demonstrated for the column with strong axis bending due to three-sided fire exposure are therefore applicable to the case in which fire exposure induces bending about the weak axis. The plastic  $P$ - $M$  interaction curve for the weak axis section will have a more circular shape and will shift less than a similar curve for a strong axis section (Garlock and Quiel, 2006).

It is interesting to note that the weak axis case endures the fire three minutes longer than the strong axis case (35 minutes versus 32 minutes, respectively), even though the weak axis flexural capacity of a section is significantly smaller than the strong axis flexural capacity. When exposed to fire on three sides, the weak axis section has less total perimeter exposed to fire (as seen in Fig. 8(a)) and will therefore have a smaller average temperature (and a larger yield strength) than the strong axis section at every time step. The strong axis section will therefore make contact with its  $P$ - $M$  capacity envelope earlier as its  $P/P_y$  ratio increases at a higher rate than that of the weak axis section.

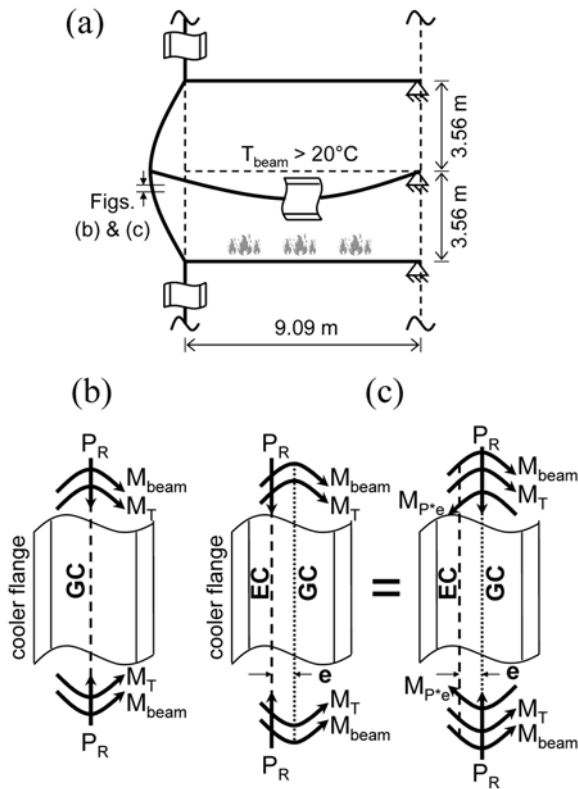


**Figure 10.** Perimeter frame behavior under fire as shown by (a) the deformed shape and by internal reactions in the section slice (b) with constant stiffness and (c) with varying stiffness.

#### 4. Frame Study

A previous study by the authors focused on the behavior of perimeter columns in a realistic high-rise building frame that experienced a severe fire (Garlock and Quiel, 2007). The prototype building frame was a moment resisting frame (MRF) composed of steel WF sections carrying a concrete floor slab on a metal deck. The study focused primarily on the fire-induced structural interaction between the columns on the perimeter of the frame with the floor beam framing into the column perpendicular to the exterior wall. A subassembly of the prototype frame is shown in Fig. 10(a) with WF section orientation and the location of the compartment fire. The fire curve shown in Fig. 3(b) was used as a realistic approximation of the actual fire event. The perimeter column was subjected to initial axial compression (through gravity loading) for which applied  $P = 15\%$  of initial  $P_y$ . The floor beam was subjected to an initial bending moment (through gravity loading) for which applied  $M = 10\%$  of initial  $M_p$  at the column face. The initial  $P/P_y$  and  $M/M_p$  values are low likely because stiffness and deflection criteria controlled the design of the frame.

Two specific analysis cases from the previous study will be examined in this paper. One case had the beams

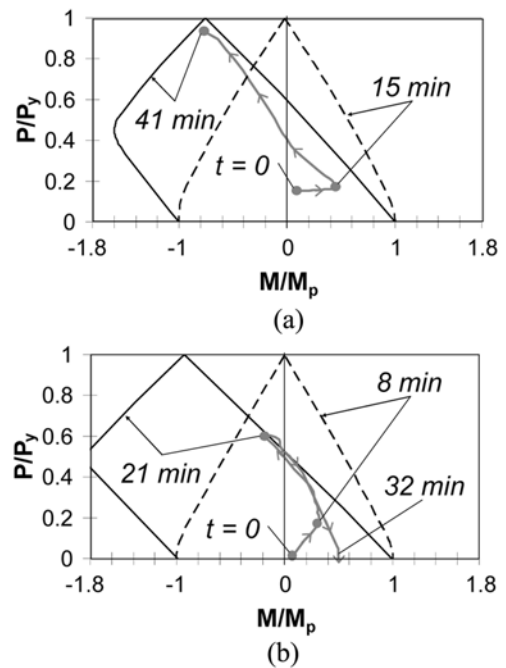


**Figure 11.** Results of the frame analysis for (a) the perimeter column in the BpCu case and (b) the floor beam in the BuCp case.

in the frame protected (i.e. coated with a code-specified thickness of fire protection material) and the columns unprotected (BpCu), and the second had the beams unprotected and the columns protected (BuCp). Details of the BpCu and BuCp analyses and models are given by (Garlock and Quiel, 2007). For both cases, the frame was discretized into beam elements (ten elements for every column length and twenty elements for every beam length) for computational structural analysis in SAFIR. This paper will examine the perimeter column at the slice shown in Fig. 10(a) (just below the expanding floor beam) as well as the floor beam at its interface with the perimeter column. The column section is a  $W14 \times 314$ , and the beam is a built-up plate girder with dimensions similar to a  $W24 \times 207$ . The nominal yield stress of the beams and columns was 250 MPa.

When the beam is heated, it expands (as shown in Fig. 10(a)) and induces a bending moment in the perimeter column (called  $M_{beam}$ ). Simultaneously, the column is heated on three sides and develops a thermal gradient. As before, this gradient induces a thermal moment  $M_T$  in the column as its thermal curvature is resisted by the rotational restraint of the continuous column ends. At “cooler” temperatures, i.e. before the steel material properties are affected by temperature, the resultant,  $P$ , of the column’s internal axial stresses acts at the GC of the perimeter column (Fig. 10(b)). When the perimeter column is heated on all sides except at the building’s exterior, the position of the EC shifts from the GC toward the cooler (i.e. exterior) flange once the material properties in the hotter flange begin to decrease (Fig. 10(c)). Since the EC

no longer coincides with the GC, another moment, opposite in direction to  $M_{beam}$  and  $M_T$ , develops when moments are measured about the GC. This moment, labeled  $M_{P^*e}$ , equals  $P$  times the eccentricity  $e$  as shown in Fig. 10(c), where  $e$  is the distance from the GC to the location of the EC. Therefore, at the time that the rate of increase of  $M_{P^*e}$  becomes larger than that of both  $M_{beam}$  and  $M_T$  combined, the total moment in the perimeter column will peak and reverse its direction. At the time that  $M_{P^*e}$  becomes greater than the combination of  $M_{beam}$  and  $M_T$ , the total moment will reverse its sign.

Fig. 11(a) shows that the normalized  $P$ - $M$  behavior for the perimeter column in the BpCu case is very similar to that of the isolated column analyses. The BpCu case is considered here so we may focus on the column's thermal response, which will be larger in this case than that of the beam. Initially, the column's  $M/M_p$  ratio increases, due primarily to an increase of both  $M_{beam}$  and  $M_T$  as the beam and column begin heating. At  $t = 15$  minutes, the rate of increase of  $M_{P^*e}$  becomes greater than that of  $M_{beam}$  and  $M_T$  combined, and the moment reverses direction. As before, the location of the peak  $M/M_p$  is well within the plastic  $P$ - $M$  interaction curve corresponding to that time. Eventually, the plastic  $P$ - $M$  interaction curve is reached at  $t = 41$  minutes following a steady increase of both  $P/P_y$  (due to a thermal reduction in yield strength) and  $M_{P^*e}$ .

The steel beams in a building are typically heated on three sides due to the presence of a concrete floor slab. The beam also develops a thermal gradient and will show a similar shift in  $y_{EC}$ ,  $y_{PC}$ , and  $y_{PNA}$  as we have shown for the isolated column bending about the strong axis. In a fire, the beam experiences a large increase in axial force since its thermal expansion is partially restrained by the perimeter column. Assuming that the reaction of this axial force acts at its GC, the beam will experience a similar axial force and moment combination as that shown in Fig. 10(c). The BuCp case is considered here so we may focus on the beam's thermal response, which will be larger in this case than that of the perimeter column. The normalized  $P$ - $M$  behavior for the BuCp beam, shown in Fig. 11(b), undergoes a moment reversal at  $t = 8$  minutes due to an increase in the growth of  $M_{P^*e}$ . As the total moment changes sign, the  $P/P_y$  ratio increases, due to both an increase in  $P$  as the beam expands and compresses and a decrease in  $P_y$  as the material heats and weakens. The plastic  $P$ - $M$  interaction curve is reached at 21 minutes, at which point the section has fully yielded through its depth. The  $P/P_y$  ratio then decreases as the member sags into a catenary position over the next couple of time steps (Garlock and Quiel, 2007). The analysis finally terminates at  $t = 32$  minutes when the final values of  $P/P_y$  ratio have just crossed into negative (tensile) axial stress.

## 5. Summary and Conclusions

This paper has presented a detailed discussion of the

behavior of steel WF sections subjected to axial loads and thermal gradients. It was shown that the effective centroid (i.e. the center of stiffness) of the section moves toward the cooler side as the temperature through the section unevenly increases. This shift of the effective centroid produces a bending moment ( $M_{P^*e}$ ) since the axial loads applied at the geometric center of the section are now acting eccentrically to the section's effective centroid. In sections with rotational restraint, this moment is opposite in direction to the moments produced by thermal strains ( $M_T$ ). Eventually, the total moment in a section with a thermal gradient (equal to  $M_{P^*e} + M_T$  + any applied moment) reverses direction due to this movement of the effective centroid.

The phenomenon described above was shown in an isolated column study as well as in a study of a frame. The isolated column study was used to evaluate the effects of increasing applied axial load on the mechanics of the shift in the section's effective centroid. It was observed that the larger the axial load, the larger the magnitude and the rate of movement of the effective centroid, and therefore the larger the subsequent moments produced by this shift. A larger applied load also produces smaller thermal moments (that are produced by the thermal strains). These two behaviors combined result in a smaller total moment in the section with larger applied load.

In the isolated column study, the effects of having the temperature gradient parallel to the web (so that *strong axis* bending develops) was compared to having the temperature gradient parallel to the flange (so that *weak axis* bending develops). Since the weak axis had a smaller moment of inertia than the strong axis, a smaller  $M_T$  develops when the gradient develops parallel to the flange. In addition, this case produces smaller movement of the effective centroid, thus leading to smaller  $M_{P^*e}$ . The magnitude of total moment that develops for the weak axis case ranges from 50-60% of the magnitude of total moment in the strong axis case, mostly due to smaller  $M_T$ .

In the frame study, the column on the building's perimeter and the beam supporting the slab are two types of elements that develop thermal gradients through the section depth and also carry axial load (the beam develops axial load due to partial restraint of its axial thermal expansion by the columns supporting it). Thus the effective centroid of both elements move towards the cooler side of the section, and  $M_{P^*e}$  subsequently develops. The overall behavior of both the perimeter column and the floor beam in the frame is the same as the isolated column.

## Acknowledgments

Mr. Quiel has been involved with this research project while on appointment as a U.S. Department of Homeland Security (DHS) Fellow under the DHS Scholarship and

Fellowship Program, a program administered by the Oak Ridge Institute for Science and Education (ORISE) for DHS through an interagency agreement with the U.S. Department of Energy (DOE). ORISE is managed by Oak Ridge Associated Universities under DOE contract number DE-AC05-00OR22750. All opinions expressed in this paper are the author's and do not necessarily reflect the policies and views of DHS, DOE, or ORISE.

## References

- Burgess I.W., El-Rimawi J.A., Plank R.J. (1990). "Analysis of beams with non-uniform temperature profile due to fire exposure." *Journal of Constructional Steel Research*, 16, pp. 169-192.
- CEN (2001). Eurocode 3: Design of steel structures, Part 1.2: General rules - Structural fire design (ENV 1993-2-2:2001). European Committee for Standardization (CEN), Brussels, Belgium.
- El-Rimawi J.A., Burgess I.W., Plank R.J. (1995). "The analysis of semi-rigid frames in fire - a secant approach." *Journal of Constructional Steel Research*, 33, pp. 125-146.
- Fletcher I., Borg A., Hitchen N., Welch S. (2006). "Performance of Concrete in Fire: Review of the State of the Art, with a Case Study of the Windsor Tower Fire." *Proc. 4<sup>th</sup> International Workshop for Structures in Fire (SiF'06)*, Vol. 2, University of Aveiro, Portugal, pp. 779-790.
- Franssen J.-M. (2005). "SAFIR: A thermal/structural program for modeling structures under fire." *Engineering Journal*, AISC, 42(3), pp. 143-158.
- Gann R.G., ed. (2005). NIST NCSTAR 1: Final report of the National Construction Safety Team on the collapse of the World Trade Center Twin Towers. Federal Building and Fire Safety Investigation of the World Trade Center Disaster, National Institute of Standards and Technology (NIST), Gaithersburg, MD.
- Garlock M.E.M., Quiel S.E. (2007). "The behavior of steel perimeter columns in a high-rise building under fire." *Engineering Journal*, AISC, 44(4).
- Garlock M.E.M., Quiel S.E. (2006). "Combined axial load and moment capacity of fire-exposed beam-columns with thermal gradients." *Proc. 4<sup>th</sup> International Workshop for Structures in Fire (SiF'06)*, Vol. 1, University of Aveiro, Portugal, pp. 187-198.
- Usmani A.S., Chung Y.C., Torero J.L. (2003). "How did the WTC Towers collapse: a new theory." *Fire Safety Journal*, 38, pp. 501-533.
- Wang Y.C. (2002). *Steel and Composite Structures: Behaviour and Design for Fire Safety*. Spon Press, London, UK.